



Correlation between the physicochemical properties and catalytic performances of $\text{Ce}_x\text{Sn}_{1-x}\text{O}_2$ mixed oxides for NO reduction by CO



Xiaojiang Yao^{a,b}, Yan Xiong^{a,b}, Weixin Zou^{a,b}, Lei Zhang^{a,b}, Shiguo Wu^{a,b}, Xian Dong^c, Fei Gao^b, Yu Deng^b, Changjin Tang^{a,b,*}, Zhuo Chen^c, Lin Dong^{a,b,*}, Yi Chen^{a,b}

^a Key Laboratory of Mesoscopic Chemistry of MOE, School of Chemistry and Chemical Engineering, Nanjing University, Nanjing 210093, PR China

^b Jiangsu Key Laboratory of Vehicle Emissions Control, Center of Modern Analysis, Nanjing University, Nanjing 210093, PR China

^c School of Chemistry and Material Science, Guizhou Normal University, Guiyang 550001, PR China

ARTICLE INFO

Article history:

Received 4 April 2013

Received in revised form 9 June 2013

Accepted 18 June 2013

Available online 27 June 2013

Keywords:

$\text{Ce}_x\text{Sn}_{1-x}\text{O}_2$ mixed oxides

Reduction behavior

Surface synergetic oxygen vacancy (SSOV)

Catalytic domain (CD)

NO reduction by CO

ABSTRACT

A series of $\text{Ce}_x\text{Sn}_{1-x}\text{O}_2$ mixed oxides and single oxides (CeO_2 and SnO_2) were prepared by inverse co-precipitation method and calcined at 450 and 750 °C to investigate the correlation between the physicochemical properties and catalytic performances of these catalysts for NO reduction by CO. The obtained samples were characterized in detail by means of XRD, UV-Raman, N_2 -physisorption, H_2 -TPR, XPS, and *in situ* DRIFTS technologies. Moreover, the catalytic performances of these samples were evaluated through NO reduction by CO model reaction. These results indicate that the incorporation of Sn^{4+} into the lattice of CeO_2 can result in the decrease of crystallite size, the increase of lattice strain and the improvement of reduction behavior, which are beneficial to the enhancement of catalytic performance. Furthermore, the catalyst with the optimal mole ratio ($\text{Ce}:\text{Sn}=2:1$) exhibits the best catalytic performance for NO reduction by CO model reaction, because that more catalytic domains (CD, $-\text{Ce}^{3+}-\square-\text{Sn}^{2+}-$ species) can be generated in the reaction process due to the enhancement of reduction behavior and the formation of uniform solid solution without crystalline SnO_2 blocking the active sites. Finally, in order to explore the significant role of catalytic domain (CD, $-\text{Ce}^{3+}-\square-\text{Sn}^{2+}-$ species) in NO reduction by CO model reaction, a possible reaction mechanism is tentatively proposed.

© 2013 Elsevier B.V. All rights reserved.

1. Introduction

The pollution of atmosphere is becoming more serious with the development of industry. As a result, the controlling emission of atmospheric pollutants is extremely urgent in order to improve the human environment. NO_x is one of the focused governance objects, which emits from stationary and mobile sources, such as coal-fired power plant and vehicle exhaust. NO reduction by CO is one of the important model reactions in three-way catalysis (TWC), which is attracting more attention of catalytic researchers due to the simultaneous elimination of NO and CO pollutant molecules [1]. It is widely reported that noble metals (Pt, Pd and Rh) supported on alumina and ceria have long been considered as the most efficient catalysts for this model reaction [2–4]. However, the practical application of supported noble metal catalysts in automobile catalytic muffler is not perfect due to their scarce, high

cost and low thermal stability [5,6]. Therefore, considerable efforts have been paid to the utilization of supported transition metal oxides, perovskites, ceria-based mixed oxides catalysts and so on for NO reduction by CO model reaction [7–9].

Recently, ceria has been widely applied in environmental catalytic field due to its high oxygen storage/release efficiency associated with the formation of oxygen vacancy and excellent reduction behavior resulted from the low redox potential between Ce^{3+} and Ce^{4+} [9–13]. However, the practical application of pure ceria is highly discouraged because of its poor thermal stability and low specific surface area [7,14]. It is widely reported that the structure modification of ceria lattice by doping with foreign metal cations (such as Zr^{4+} , Hf^{4+} , Ti^{4+} , Al^{3+} , Mg^{2+} and Mn^{x+}) may increase the specific surface area, enhance the reduction behavior and improve the thermal stability effectively [10,12,15–17]. According to the literatures, the dissociation of NO is the key step in NO reduction by CO model reaction, and oxygen vacancy can activate the N–O bond to promote the dissociation of NO species [18–20]. With regard to CeO_2 , in order to improve its catalytic performance in this model reaction, it is necessary to enhance the reduction behavior of CeO_2 by introducing suitable foreign metal cations, because that the enhancement of reduction behavior is

* Corresponding authors at: School of Chemistry and Chemical Engineering, Nanjing University, Hankou Road 22#, Nanjing, Jiangsu 210093, PR China.

Tel.: +86 25 83592290; fax: +86 25 83317761.

E-mail addresses: tangcj@nju.edu.cn (C. Tang), donglin@nju.edu.cn (L. Dong).

beneficial to the formation of more oxygen vacancies during the reaction process. Hegde et al. reported that the incorporation of Sn^{4+} into the lattice of CeO_2 to form $\text{Ce}_x\text{Sn}_{1-x}\text{O}_2$ mixed oxides can improve its reduction behavior more effective than other foreign metal cations doping, owing to the two electrons exchange between $\text{Ce}^{4+}/\text{Ce}^{3+}$ and $\text{Sn}^{4+}/\text{Sn}^{2+}$ redox couples through the redox equilibrium of $2\text{Ce}^{3+} + \text{Sn}^{4+} \leftrightarrow 2\text{Ce}^{4+} + \text{Sn}^{2+}$ [21]. It is easy to understand the formation of $-\text{Ce}^{4+}-\text{O}-\text{Sn}^{4+}-$ species in $\text{Ce}_x\text{Sn}_{1-x}\text{O}_2$ mixed oxides by electron interaction. Furthermore, the bridge oxygen of $-\text{Ce}^{4+}-\text{O}-\text{Sn}^{4+}-$ species can be removed by CO to generate $-\text{Ce}^{3+}-\square-\text{Sn}^{2+}-$ species (\square represents surface synergetic oxygen vacancy (SSOV)) during the reaction process, and the surface Ce^{3+} is conducive to the adsorption and activation of CO species [19,22,23]. As a result, we believe that the catalytic domain (CD, $-\text{Ce}^{3+}-\square-\text{Sn}^{2+}-$ species) is bound to result in excellent catalytic performance for NO reduction by CO model reaction due to the synergistic effect between surface Ce^{3+} and surface synergetic oxygen vacancy (SSOV).

In the present work, a series of $\text{Ce}_x\text{Sn}_{1-x}\text{O}_2$ mixed oxides with different mole ratio of Ce:Sn were prepared by inverse co-precipitation method, and calcined at 450 and 750 °C, respectively. And then, these obtained samples were characterized by means of XRD, UV-Raman, N_2 -physisorption, H_2 -TPR, XPS, and *in situ* DRIFTS technologies. Furthermore, NO reduction by CO as a model reaction was carried out to evaluate the catalytic performances of these samples. This study is mainly focused on: (1) investigating the correlation between physicochemical properties and catalytic performances of these $\text{Ce}_x\text{Sn}_{1-x}\text{O}_2$ mixed oxides; (2) approaching the possible reaction mechanism of NO reduction by CO model reaction through investigating the interaction of CO or/and NO with these catalysts by *in situ* DRIFTS technique in the temperature range of 25–400 °C; (3) exploring the role of catalytic domain (CD, $-\text{Ce}^{3+}-\square-\text{Sn}^{2+}-$ species) in NO reduction by CO model reaction.

2. Experimental

2.1. Catalysts preparation

The $\text{Ce}_x\text{Sn}_{1-x}\text{O}_2$ mixed oxides (Ce:Sn = 4:1, 2:1, 1:1, 1:2 mole ratio) were prepared from their salt solutions as precursors by inverse co-precipitation method [9]. In detail, the desired quantities of ammonium cerium (IV) nitrate and tin (IV) tetrachloride were dissolved in distilled water separately and mixed together for magnetic stirring 2 h, and then slowly added into the excess ammonia (25%) with vigorously stirring until pH = 10. The resulting suspension was kept in stirring for another 3 h, aged 24 h, and then filtered, washed several times with distilled water until no pH changed and no Cl^- detected by the solution of AgNO_3 . The obtained cake was oven dried at 110 °C for 12 h and finally calcined at 450 and 750 °C in the flowing air for 5 h, respectively. In addition, pure CeO_2 and SnO_2 were prepared by a similar way for comparison. These synthesized samples are denoted as CxSy-450 (750), for example, C2S1-450 represents that the mole ratio of Ce:Sn is 2:1 and the calcination temperature is 450 °C.

2.2. Catalysts characterization

X-ray diffraction (XRD) patterns were recorded on a Philips X'pert Pro diffractometer using Ni-filtered $\text{Cu K}\alpha$ radiation ($\lambda = 0.15418$ nm). The X-ray tube was operated at 40 kV and 40 mA. The intensity data were collected over a 2θ range of 10–80°. The scan speed was set at 10°min^{-1} with a step size of 0.02° . The mean crystallite size (D_β) from the strongest peak and lattice strain (ε) of

these samples were determined by $D_\beta = K\lambda/\beta \cos \theta$ (Debye-Scherrer equation) and $\varepsilon = \beta/4\lg \theta$, respectively, where K is the particle shape factor, usually taken as 0.89, λ is the X-ray wavelength, β is the full-width at half maximum height (FWHM) in radians, and θ is the diffraction angle.

UV-Raman spectra were collected on a Renishaw UV-vis Raman System 1000 spectrometer equipped with a CCD detector. The 325 nm of the He–Cd laser was used as the exciting source with power of 5 mW measured at the analysis spot.

Textural characteristics of these samples were obtained by N_2 -physisorption at -196°C on a Micromeritics ASAP-2020 analyzer, using the Brunauer–Emmett–Teller (BET) method for the specific surface area and the Barrett–Joyner–Halenda (BJH) method for the pore distribution. Prior to each analysis, the catalyst was degassed under vacuum at 300 °C for 4 h.

H_2 -temperature programmed reduction (H_2 -TPR) experiments were performed in a quartz U-type reactor connected to a thermal conductivity detector (TCD) with Ar– H_2 mixture (7.0% of H_2 by volume, 70 ml min^{-1}) as a reductant. Prior to the reduction, the sample (50 mg) was pretreated in a high purified N_2 stream at 300 °C for 1 h and then cooled to room temperature. After that, the TPR started from 50 °C to target temperature at a rate of $10^\circ\text{C min}^{-1}$.

X-ray photoelectron spectroscopy (XPS) analysis was performed on a PHI 5000 VersaProbe system, using monochromatic Al $\text{K}\alpha$ radiation (1486.6 eV) operating at an accelerating power of 15 kW. Before the measurement, the sample was outgassed at room temperature in a UHV chamber ($<5 \times 10^{-7}$ Pa). The sample charging effects were compensated by calibrating all binding energies (BE) with the adventitious C 1s peak at 284.6 eV. This reference gave BE values with accuracy at ± 0.1 eV.

In situ diffuse reflectance infrared Fourier transform spectra (*in situ* DRIFTS) were collected from 650 to 4000 cm^{-1} at a spectral resolution of 4 cm^{-1} (number of scans, 32) on a Nicolet 5700 FT-IR spectrometer equipped with a high-sensitive MCT detector cooled by liquid N_2 . The DRIFTS cell (Harrick) was fitted with a ZnSe window and a heating cartridge that allowed sample to be heated to 400 °C. The fine catalyst powder placed on a sample holder was carefully flattened to enhance IR reflection. The sample was pretreated with a high purified N_2 stream at 400 °C for 1 h to eliminate the physisorbed water and other impurities. The sample background of each target temperature was collected during the cooling process. At ambient temperature, the sample was exposed to a controlled stream of CO–Ar (10% of CO by volume) or NO–Ar (5% of NO by volume) at a rate of 5.0 ml min^{-1} for 1 h to be saturated. Desorption/reaction studies were performed by heating the adsorbed species and the spectra were recorded at various target temperatures at a rate of $10^\circ\text{C min}^{-1}$ from room temperature to 400 °C by subtraction of the corresponding background reference.

2.3. Catalytic performances measurement

The catalytic performances of these catalysts for NO reduction by CO model reaction were determined under steady state, involving a feed stream with a fixed composition, 5% NO, 10% CO and 85% He by volume as diluents. The sample (50 mg) was fitted in a quartz tube and pretreated in a high purified N_2 stream at 300 °C for 1 h and then cooled to room temperature, after that, the mixed gases were switched on. The reactions were carried out at different temperatures with a space velocity of $12,000 \text{ ml g}^{-1} \text{ h}^{-1}$. Two columns (length, 1.75 m; diameter, 3 mm) and two thermal conductivity detectors ($T = 100^\circ\text{C}$) were used for analyzing the products. Column A with Paropak Q for separating CO_2 and N_2O , column B packed with 5A and 13X molecule sieve (40–60 M) for separating N_2 , NO and CO.

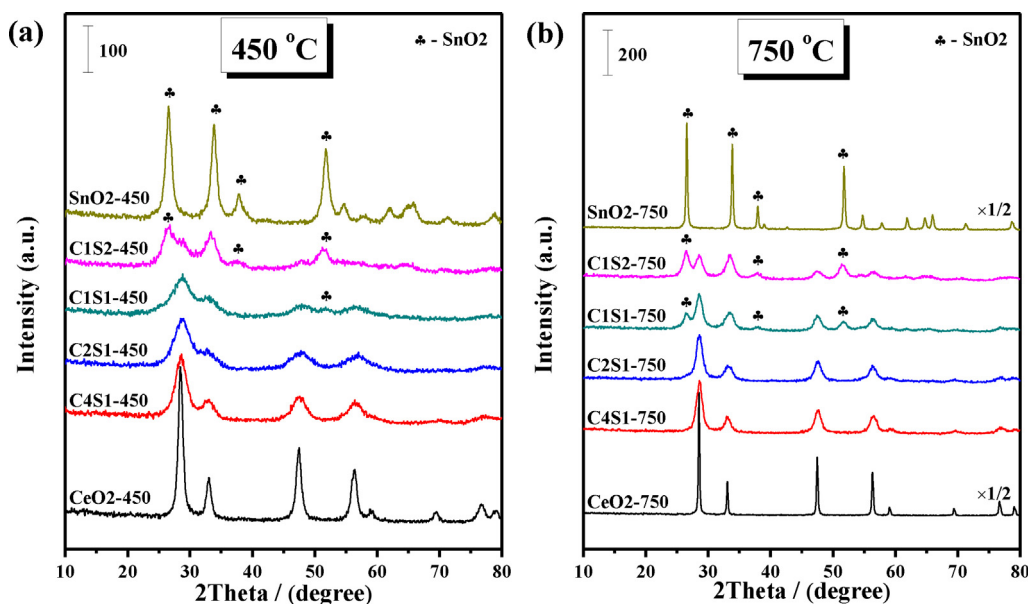


Fig. 1. The XRD patterns of these $\text{Ce}_x\text{Sn}_{1-x}\text{O}_2$ mixed oxides calcined at 450 and 750 °C, respectively.

3. Results and discussion

3.1. Structural characteristics (XRD and UV-Raman)

Fig. 1 displays the XRD patterns of these $\text{Ce}_x\text{Sn}_{1-x}\text{O}_2$ mixed oxides calcined at 450 and 750 °C, respectively. It can be seen from Fig. 1a, for the samples calcined at 450 °C, only the broad diffraction lines attributed to cubic fluorite-type phase CeO_2 (PDF-ICDD 34-0394) are detected, without extra characteristic lines assigned to SnO_2 when the mole ratio of Ce:Sn is no less than 2:1. Furthermore, the diffraction peaks of C4S1-450 and C2S1-450 are shifted to high angle direction slightly compared with CeO_2 -450, indicating that Sn^{4+} has been successfully incorporated into the lattice of CeO_2 to form uniform solid solution (containing $-\text{Ce}^{4+}-\text{O}-\text{Sn}^{4+}$ -species) maintaining the cubic fluorite-type structure, which is in agreement with the literatures [9,10,21]. Increasing the content of Sn^{4+} (Ce:Sn \leq 1:1), the similar phenomena can be observed, and a series of new diffraction peaks assigned to tetragonal rutile structure SnO_2 (PDF-ICDD 41-1445) appear at the corresponding positions, demonstrating that besides part of Sn^{4+} has been incorporated into the lattice of CeO_2 , the other exists in the form of crystalline SnO_2 . Compared with CeO_2 -450, the diffraction peaks of these $\text{Ce}_x\text{Sn}_{1-x}\text{O}_2$ -450 mixed oxides are broadened due to crystallite nanodimensions effect [24,25], as evidenced by the crystallite size of these samples determined from the diffraction peak of the (1 1 1) plane by Debye–Scherrer equation (listed in Table 1). In general, the crystallite size of these $\text{Ce}_x\text{Sn}_{1-x}\text{O}_2$ -450 mixed oxides is smaller than that of CeO_2 -450, which may be caused by the introduction of Sn^{4+} into the lattice of CeO_2 , and further inhibits the crystal growth of the cubic phase [9,17]. In addition, it can be seen from Table 1, the lattice parameter of these $\text{Ce}_x\text{Sn}_{1-x}\text{O}_2$ -450 mixed oxides is smaller than that of CeO_2 -450 (5.4200 Å), which is primarily due to that the ionic radius of Sn^{4+} (0.71 Å) is smaller than that of Ce^{4+} (0.92 Å), the incorporation of Sn^{4+} into the lattice of CeO_2 leads to contraction and distortion of the lattice [9,10,21,26,27]. Finally, the introduction of Sn^{4+} results in the extra force which increases the lattice strain of CeO_2 (Table 1). As reported previously, lattice strain was a measurement of the lattice stress existing in the materials resulted from surface effects and/or crystal imperfections [28,29]. Therefore, the above difference in lattice strain may

be related to surface effects and/or the concentration of oxygen vacancy in these samples [28].

With increasing the calcination temperature from 450 to 750 °C (Fig. 1b), a remarkable increase in the intensity of the diffraction peaks of cubic fluorite-type phase CeO_2 and tetragonal rutile structure SnO_2 due to better crystallization can be found. Moreover, the variation of crystallite size, lattice parameter and lattice strain is very similar with the samples calcined at 450 °C (Table 1). However, with regard to C4S1-750 and C2S1-750 samples, no obvious phase separation of SnO_2 from CeO_2 is observed, indicating that their thermal stability is very good.

It is well known that the gas-solid reactions usually take place on the surface of the catalysts. As a result, the understanding of the surface information of the catalysts is very important. XRD as a bulk characterization reflects the surface structure of the samples rarely, and it can be well complemented by Raman spectroscopy, which can detect the surface information of the samples effectively. It is widely reported that the Raman spectrum of CeO_2 exhibited a main band at 464 cm^{-1} corresponding the F_{2g} vibration model of the cubic fluorite type CeO_2 lattice and two weak bands around 300 and 600 cm^{-1} linked to the presence of oxygen vacancy in CeO_2 lattice [9,15,24]. According to the literature, as the UV laser line (325 nm) is used, the bands around 300 and 600 cm^{-1} can be strengthened due to its shallower depth of sample detecting and oxygen vacancy enriched at the surface of the sample, which is beneficial to calculate the concentration of oxygen vacancy [13]. Therefore, the UV-Raman spectra of these samples calcined at 450 and 750 °C are recorded and shown in Fig. 2. We can find that all these $\text{Ce}_x\text{Sn}_{1-x}\text{O}_2$ mixed oxides calcined at 450 °C display three bands labeled I, II, and III, which is similar with CeO_2 -450 (Fig. 2a). Especially, the F_{2g} vibration model (in the region II) of these $\text{Ce}_x\text{Sn}_{1-x}\text{O}_2$ -450 mixed oxides shifts to low wavenumber direction slightly compared with CeO_2 -450, indicating that the introduction of Sn^{4+} can change the surface structure of CeO_2 to form $-\text{Ce}^{4+}-\text{O}-\text{Sn}^{4+}$ -species (Table 1). Moreover, some researchers reported that the sum of the peak area of the bands I and III divided by the peak area of the band II (i.e., $(A_I + A_{III})/A_{II}$) can reflect the concentration of oxygen vacancy [6,9,30]. However, SnO_2 -450 exhibits four bands (E_u , E_g , A_{1g} , and B_{2g}) at 346, 478, 630, and 740 cm^{-1} , respectively [31–33]. The overlaps of E_u and band I, A_{1g} and band III cause us

Table 1Crystallite size, lattice parameter, lattice strain and the position of the main UV-Raman line (F_{2g}) of these $Ce_xSn_{1-x}O_2$ mixed oxides calcined at 450 and 750 °C, respectively.

Catalysts	Crystallite size (nm)	Lattice parameter (Å)	Lattice strain (%)	Position of F_{2g} (cm^{-1})
CeO ₂ -450	15.0	5.4200	0.60	464
C4S1-450	4.6	5.4024	0.78	460
C2S1-450	3.4	5.3759	1.05	456
C1S1-450	3.0	5.3666	1.17	456
C1S2-450	–	–	1.27	456
SnO ₂ -450	7.1	$a = b = 4.7473, c = 3.1894$	0.35	–
CeO ₂ -750	50.6	5.4143	0.15	465
C4S1-750	14.5	5.3986	0.33	461
C2S1-750	10.7	5.3698	0.39	458
C1S1-750	10.2	5.3602	0.46	458
C1S2-750	8.3	5.3591	0.66	458
SnO ₂ -750	35.0	$a = b = 4.7404, c = 3.1880$	0.18	–

cannot calculate the concentration of oxygen vacancy accurately. Fortunately, it can be seen from the intensity of the bands I, III, E_u , and A_{1g} in these samples that the introduction of Sn^{4+} can increase the oxygen vacancy concentration of CeO₂ to some extent. Fig. 2b presents the UV-Raman spectra of the samples calcined at 750 °C. From this figure, we can find that the oxygen vacancy concentration of these $Ce_xSn_{1-x}O_2$ -750 mixed oxides is smaller than that of $Ce_xSn_{1-x}O_2$ -450 mixed oxides owing to the calcination at high temperature.

3.2. Textural characteristics (N_2 -physisorption)

Fig. 3 exhibits N_2 adsorption–desorption isothermal plots and the corresponding BJH pore size distribution curves of these samples calcined at 450 and 750 °C, respectively. It can be seen from Fig. 3a that the isotherms of these samples calcined at 450 °C are of classical type IV as defined by IUPAC [34], which is characteristic of mesoporous materials due to the textural of inter-particle mesoporosity. A well-defined H2-type hysteresis loop with a sloping adsorption branch and a relatively steep desorption branch is observed at high relative pressure range (P/P_0) for every sample. This H2-type hysteresis loop is typical for wormhole-like mesostructure and interstice mesoporous structure formed by

nanoparticle assembly [6,14]. Furthermore, the pore size distribution curves of these samples determined by the BJH method from adsorption branch of the corresponding isotherms exhibit one single narrow peak centered at 2.88–11.03 nm, indicating that these samples possess uniform mesopore size distributions (Fig. 3c). The samples calcined at 750 °C also show classical type IV isotherm with H2-type hysteresis loop except SnO₂-750 (Fig. 3b). The average pore diameter of these samples is larger than the corresponding samples calcined at 450 °C due to the growth of grain (Fig. 3d).

The textural data of these samples calcined at 450 and 750 °C are listed in Table 2. Compared with pure CeO₂, when Sn^{4+} is doped into the lattice of CeO₂, both the specific surface area and pore volume are increased, which is beneficial to the contact with the reactant molecules and further to improve the catalytic performance. These changes may be related to the crystallite size of these samples to some extent. In other words, the incorporation of Sn^{4+} into the lattice of CeO₂ can improve the textural property effectively. Interestingly, compared with pure CeO₂, the degree of sintering (i.e., $(S_{BET}(450) - S_{BET}(750))/S_{BET}(450)$) is smaller when Sn^{4+} incorporates into the lattice of CeO₂, indicating that the ability of anti-sintering of CeO₂ is enhanced with the introduction of Sn^{4+} . Especially, C2S1-450 sample exhibits the largest BET specific surface area and the best anti-sintering ability, which may be due

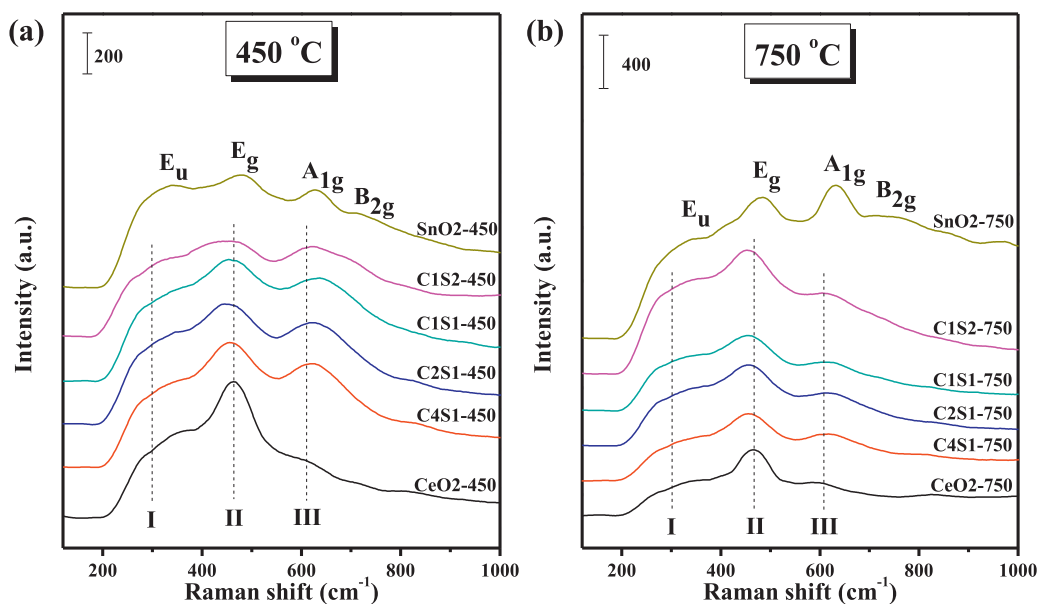


Fig. 2. The UV-Raman spectra of these $Ce_xSn_{1-x}O_2$ mixed oxides calcined at 450 and 750 °C, respectively.

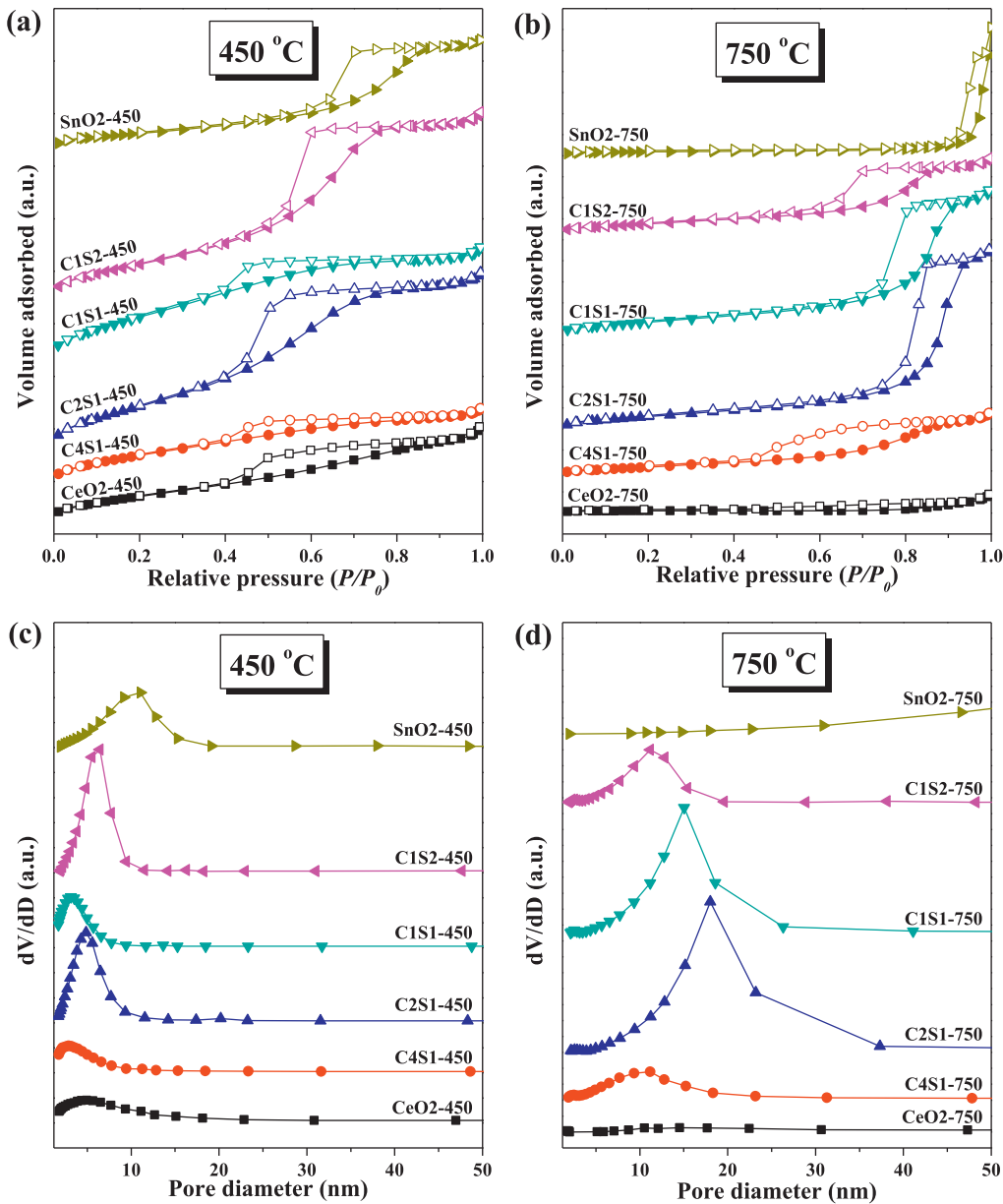


Fig. 3. The N₂ adsorption–desorption isotherms and BJH pore distribution curves of these Ce_xSn_{1–x}O₂ mixed oxides calcined at 450 and 750 °C, respectively.

Table 2
The textural properties of these Ce_xSn_{1–x}O₂ mixed oxides calcined at 450 and 750 °C, respectively.

Sample	BET surface area (m ² g ^{–1})	Pore volume (cm ³ g ^{–1})	Average pore diameter (nm)	(S _{BET} (450)–S _{BET} (750))/S _{BET} (450)
CeO ₂ -450	65.7	0.073	4.93	–
C4S1-450	82.0	0.065	2.88	–
C2S1-450	123.5	0.145	4.87	–
C1S1-450	122.4	0.098	3.16	–
C1S2-450	102.3	0.150	6.44	–
SnO ₂ -450	38.6	0.082	11.03	–
CeO ₂ -750	3.8	0.010	14.54	0.9422
C4S1-750	24.7	0.047	11.17	0.6988
C2S1-750	38.9	0.138	18.01	0.6850
C1S1-750	38.5	0.111	15.05	0.6855
C1S2-750	27.2	0.056	11.19	0.7341
SnO ₂ -750	6.5	0.028	75.36	0.8316

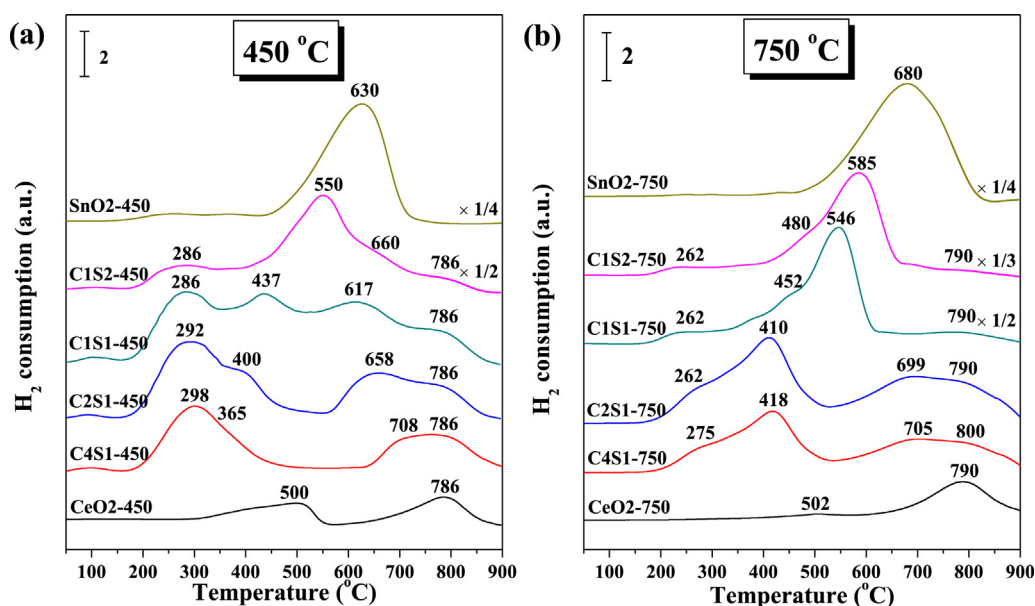


Fig. 4. H_2 -TPR profiles of these $Ce_xSn_{1-x}O_2$ mixed oxides calcined at 450 and 750 °C, respectively.

to its uniform solid solution structure without the covering of crystalline SnO_2 .

3.3. Reduction properties (H_2 -TPR)

The reduction properties of these samples calcined at 450 and 750 °C are characterized by H_2 -TPR, and the results are shown in Fig. 4. It can be seen from Fig. 4a that CeO_2 -450 exhibits two reduction peaks around 500 and 786 °C, which is assigned to the reduction of surface CeO_2 and bulk CeO_2 , respectively [15,35]. Moreover, a strong reduction peak locates at 630 °C for SnO_2 -450, and the final product is Sn^0 metal [9,36]. However, Hegde et al. reported that Sn^{4+} in $Ce_{0.6}Sn_{0.4}O_2$ solid solution could be reduced to Sn^{2+} by H_2 up to 550 °C through XPS measurement [21]. Interestingly, all of the $Ce_xSn_{1-x}O_2$ -450 mixed oxides show four reduction peaks, which may be related to the reduction of $-Ce^{4+}-O-Ce^{4+}$, $-Ce^{4+}-O-Sn^{4+}$, $-Sn^{4+}-O-Sn^{4+}$ species and the further reduction of Sn^{2+} to Sn^0 metal [9,21]. Besides, these reduction peaks shift to low-temperature direction obviously, which is resulted from the strong interaction between Ce^{4+}/Ce^{3+} and Sn^{4+}/Sn^{2+} through the redox equilibrium of $2Ce^{3+} + Sn^{4+} \leftrightarrow 2Ce^{4+} + Sn^{2+}$, indicating that the oxygen atoms of the $Ce_xSn_{1-x}O_2$ -450 mixed oxides are easier to migrate to generate oxygen vacancy during the reduction process. Furthermore, the quantitative H_2 -TPR results (Table 3) display that the actual H_2 consumption of these $Ce_xSn_{1-x}O_2$ -450 mixed oxides is larger than the corresponding estimated H_2 consumption, demonstrating that the introduction of Sn^{4+} can promote the reduction of CeO_2 , which is similar with the results of Hegde et al. [21].

It can be seen from Fig. 4b that CeO_2 -750 also shows two reduction peaks, but the reduction of surface CeO_2 is weakened due to high-temperature calcination. Interestingly, the reduction peaks of $C4S1$ -750 and $C2S1$ -750 are very similar with $C4S1$ -450 and $C2S1$ -450, demonstrating that these samples possess good thermal stability, which is in agreement with the XRD results. In addition, $C1S1$ -750 and $C1S2$ -750 exhibit different reduction behavior from the corresponding samples calcined at 450 °C, which may be related to the partial separation of SnO_2 from CeO_2 . However, the quantitative H_2 -TPR results (Table 3) indicate that there is still some strong interaction between Ce^{4+}/Ce^{3+} and Sn^{4+}/Sn^{2+} for these $Ce_xSn_{1-x}O_2$ -750 mixed oxides, but their reduction properties are inferior to

the corresponding samples calcined at 450 °C due to the sintering effect.

3.4. Catalytic performances ($NO + CO$ model reaction)

Fig. 5 displays the activities and selectivities of NO reduction by CO model reaction over these samples calcined at 450 and 750 °C, respectively. From Fig. 5a and c, we can find that the single oxides CeO_2 -450 and SnO_2 -450 exhibit poor catalytic performances. However, the incorporation of Sn^{4+} into the lattice of CeO_2 can enhance the activity and selectivity for this model reaction remarkably, especially that $C2S1$ -450 exhibits the best catalytic performance among these samples. The possible reason is that: firstly, according to the XRD results, the incorporation of Sn^{4+} into the lattice of CeO_2 inhibits the crystal growth of the cubic phase, resulting in the increase of lattice strain and the decrease of crystallite size. It is well known that the larger lattice strain of the catalyst is beneficial to the activation of reactant molecules, and further enhances the catalytic performance [28,29]. Some researchers reported that the decrease of crystallite size caused the enlargement of BET specific surface area and the increase of surface Ce^{3+} , the former was conducive

Table 3

The actual and theoretical H_2 consumption of these $Ce_xSn_{1-x}O_2$ mixed oxides calcined at 450 and 750 °C, respectively.

Samples	H_2 consumption ($\mu\text{mol/g}$)	
	Experimental amount	Estimated amount ^a
CeO_2 -450	766	–
$C4S1$ -450	2788	2561
$C2S1$ -450	4242	3757
$C1S1$ -450	5883	5253
$C1S2$ -450	7742	6749
SnO_2 -450	9740	–
CeO_2 -750	390	–
$C4S1$ -750	2386	2261
$C2S1$ -750	4168	3508
$C1S1$ -750	5762	5067
$C1S2$ -750	7538	6626
SnO_2 -750	9744	–

^a Estimated amounts of $Ce_xSn_{1-x}O_2$ mixed oxides were determined from the H_2 consumption of CeO_2 and SnO_2 : $766x + 9740(1-x)$ and $390x + 9744(1-x)$ for the samples calcined at 450 °C and 750 °C, respectively.

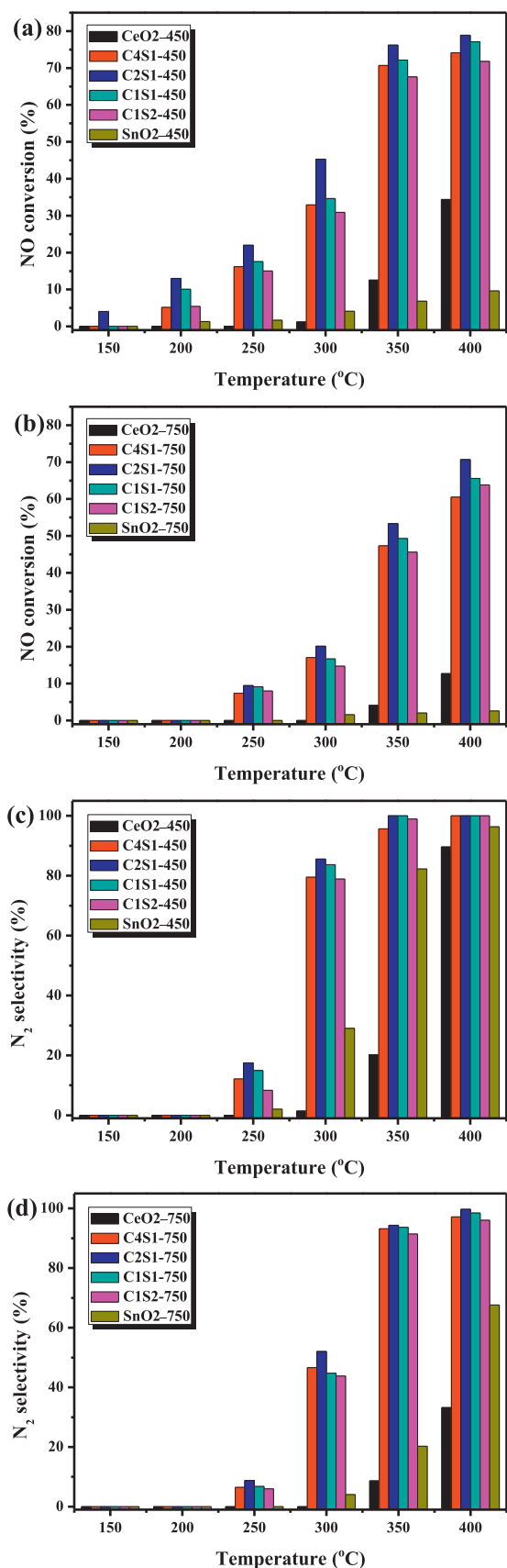


Fig. 5. (a, b) NO conversions and (c, d) N_2 selectivities of these $Ce_xSn_{1-x}O_2$ mixed oxides calcined at 450 and 750 °C, respectively.

to the sufficient contact between catalyst and reactant molecules, the latter contributed to the adsorption of CO_x species, which further promoted the catalytic performance [22,23,37–40]. Secondly, H_2 -TPR results demonstrate that the incorporation of Sn^{4+} into the lattice of CeO_2 can enhance its reduction property obviously. In other words, these $Ce_xSn_{1-x}O_2$ mixed oxides can be easier reduced by CO in the reaction gases to form more oxygen vacancies and Ce^{3+} . Furthermore, the oxygen vacancy can weaken the N–O bond to promote the dissociation of NO_x , which is beneficial to the enhancement of the catalytic performance [20]. Interestingly, we can find that when the mole ratio of Ce:Sn is no less than 2:1, the activity and selectivity elevate with the increase of Sn^{4+} content due to the formation of more $-Ce^{4+}-O-Sn^{4+}-$ species. However, if the mole ratio of Ce:Sn is lower than 2:1, the catalytic performance declines with the further increase of Sn^{4+} content, because that the redundant Sn^{4+} existing in the form of crystalline SnO_2 blocks the active sites of the catalyst. Fig. 5b and d show that the catalytic performances of these $Ce_xSn_{1-x}O_2$ -750 mixed oxides are also better than the single oxides CeO_2 -750 and SnO_2 -750. However, the catalytic performances of the samples calcined at 750 °C are inferior to the corresponding samples calcined at 450 °C due to the sintering effect.

3.5. Chemical states analysis (XPS)

In order to further investigate the elementary oxidation states and surface compositions of these synthesized samples, XPS is carried out over some representative samples (i.e., CeO_2 -450, C2S1-450, C2S1-750 and SnO_2 -450), and the corresponding results are displayed in Fig. 6. The complex spectrum of Ce 3d for these samples is decomposed into eight components with the assignment defined in Fig. 6a. According to the literatures, the bands labeled u' and v' represent $3d^{10}4f^1$ initial electronic state corresponding to Ce^{3+} , while the other six bands labeled u'' and v'' , u' and v' , u and v are related to Ce^{4+} [9,41,42]. Therefore, the chemical valence of cerium on the surface of these samples is mainly in a +4 oxidation state, and a small amount of Ce^{3+} co-exists. Moreover, from the area of these peaks, the contents of Ce^{3+} relative to the total Ce concentration of these samples are calculated by the following equation [43]:

$$Ce^{3+} (\%) = \frac{S_{u'} + S_{v'}}{\sum (S_{u'} + S_{v'})} \times 100$$

The contents of Ce^{3+} calculated for these samples are listed in Table 4. It can be seen from this table that the contents of Ce^{3+} of C2S1-450 and C2S1-750 are larger than that of CeO_2 -450. There are two possible reasons, the first is that the substitution of Ce^{4+} ($r=0.92$ Å) by Sn^{4+} ($r=0.71$ Å) in the lattice of CeO_2 will lead to the contraction of the lattice, while the spontaneous transformation of Ce^{4+} ($r=0.92$ Å) into the larger Ce^{3+} ($r=1.03$ Å) can compensate for this lattice contraction [28]; the second is that the fraction of Ce^{3+} in the particles increases with the crystallite size decreasing [39,40], which is supported by the XRD results. Furthermore, the content of Ce^{3+} of C2S1-750 is smaller than that of C2S1-450 due to its larger crystallite size and more sufficient oxidation at high temperature.

The spectrum of Sn 3d of these representative samples is numerically fitted with two components, as shown in Fig. 6b. The binding energies of Sn $3d_{5/2}$ and Sn $3d_{3/2}$ of SnO_2 are at 486.9 and 495.3 eV, respectively [21]. Interestingly, the Sn $3d_{5/2}$ and Sn $3d_{3/2}$ peaks of C2S1-450 and C2S1-750 appear at lower binding energies compared with SnO_2 -450, indicating that there are excess electrons around Sn in C2S1-450 and C2S1-750, and further demonstrating the existence of synergistic interaction between Ce and Sn through the redox equilibrium of $2Ce^{3+} + Sn^{4+} \leftrightarrow 2Ce^{4+} + Sn^{2+}$. In

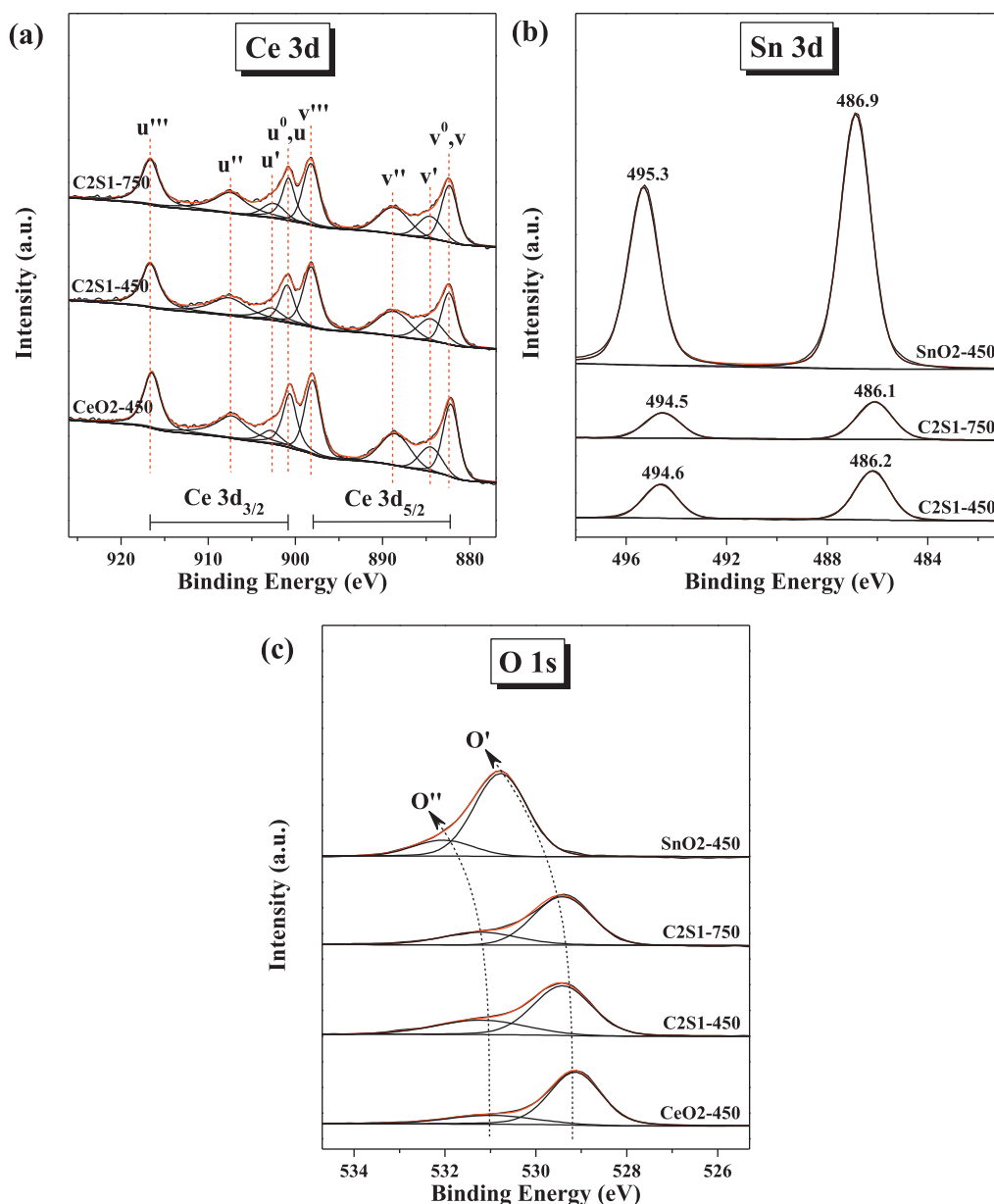


Fig. 6. XPS spectra ((a) Ce 3d, (b) Sn 3d and (c) O 1s) of the representative samples.

addition, the surface atomic concentration and atomic ratio of these representative samples obtained by XPS analysis are also summarized in Table 4. The surface Ce/Sn atomic ratio of C2S1-450 and C2S1-750 is higher than the nominal ratio as indicated by the value in parentheses, which suggests that a large number of Sn has incorporated into the bulk CeO_2 lattice. Interestingly, the surface Ce/Sn atomic ratio of C2S1-750 is larger than that of C2S1-450, demonstrating that more Sn can penetrate into the bulk CeO_2 lattice due to high temperature calcination.

The high-resolution spectrum for the O 1s ionization features of these representative samples is numerically fitted with two components representing the primary O 1s ionization feature and chemically shifted O 1s feature from chemisorbed surface species, which is exhibited in Fig. 6c. CeO_2 -450 shows a main peak (O') at 529.1 eV and a shoulder (O'') with higher binding energy at 531.0 eV, the former is attributed to the characteristic lattice oxygen bonding to metal cations, while the latter is considered as the adsorbed oxygen and oxygen in carbonates, hydroxyl

Table 4

The surface compositions of the representative samples obtained by XPS analysis.

Catalysts	Atomic concentration				Atomic ratio			
	C (at%)	Ce (at%)	Sn (at%)	O (at%)	Ce/Sn	O/(Ce+Sn)	$S_{O'}/(S_{O'} + S_{O''})$ (%)	$(S_{O'} + S_{O''})/S_{\text{total}}$ (%)
CeO_2 -450	28.75	20.77	–	50.48	–	2.43 (2.00)	21.77	11.76
C2S1-450	23.18	15.36	6.68	54.78	2.30 (2.00)	2.49 (2.00)	29.93	15.56
C2S1-750	22.67	17.40	5.66	54.27	3.07 (2.00)	2.35 (2.00)	27.58	13.17
SnO_2 -450	6.79	–	29.57	63.64	–	2.15 (2.00)	17.17	–

groups [6,15,30]. Moreover, C2S1-450, C2S1-750 and SnO₂-450 also exhibit two peaks (O' and O'') in Fig. 6c. However, we can find that the binding energy of O 1s in these samples is higher than that of CeO₂-450. The reason may be that the electronegativity of Sn (1.96) is larger than that of Ce (1.10), i.e., the capturing electrons ability of Sn is stronger than that of Ce, which leads to the higher binding energy of O 1s in C2S1-450, C2S1-750 and SnO₂-450 compared with CeO₂-450 due to the smaller electron density around O element [6]. Furthermore, Table 4 shows that the O/(Ce+Sn) ratio for these representative samples is higher than the nominal ratio (2.00) of the full oxidation state, the excess surface oxygen may be assigned to high concentration of surface oxygen as an adsorbed layer of CO₂, CO or water [28,44]. The relative percentage of these two kinds of oxygen species (i.e., lattice oxygen and chemisorbed oxygen) is quantified based on the area of O' and O'', the proportion of $S_{O'}/(S_{O'} + S_{O''})$ for these samples follows the order: CeO₂-450 < C2S1-750 < C2S1-450, which is in accordance with the order of the relative content of surface Ce³⁺, indicating that CO₂ and CO can interact with Ce³⁺ sites easier than those with Ce⁴⁺ sites. This observation is similar with some reported results that CO₂ and CO could be adsorbed on the reduced state Ce³⁺ sites more effective than those on the oxidized state Ce⁴⁺ sites [22,23].

3.6. CO or/and NO interaction with these representative samples (in situ DRIFTS)

The *in situ* DRIFTS of CO adsorption are carried out at various temperatures to understand the adsorption and reduction properties of these representative samples, and the corresponding results are exhibited in Fig. 7. With regard to the exposure of CeO₂-450 to CO at room temperature, it is widely reported that the bands at about 1029, 1301 and 1475 cm⁻¹ are the different vibration modes of monodentate carbonates, i.e., $\nu(\text{C}-\text{O})$, $\nu_s(\text{CO}_3^{2-})$ and $\nu_{as}(\text{CO}_3^{2-})$; the band at ~1208 cm⁻¹ is attributed to hydrogencarbonates with $\delta(\text{C}-\text{O}\cdots\text{H})$ vibration mode; the bands at ca. 1383 and 1568 cm⁻¹ are ascribed to $\nu_s(\text{COO}^-)$ and $\nu_{as}(\text{COO}^-)$ vibration modes of carboxylates; and the twin bands at about 2118 and 2172 cm⁻¹ are resulted from the P-branch and R-branch of gaseous CO [45–48]. We can find that with the increase of temperature to 250 °C, the band at 1029 cm⁻¹ disappears due to the thermal desorption and reduction, and a new band for CO_x coordinated to the reduced ceria appears at 1058 cm⁻¹, indicating that CeO₂-450 can be reduced by CO during the heating process [49]. Moreover, further raising the temperature leads to the bands assigned to these carbonates and carboxylates enhance because the adsorption of CO and CO₂ on the reduced state Ce³⁺ sites is more effective than those on the oxidized state Ce⁴⁺ sites [22,23]. For C2S1-450, the bands of monodentate carbonates, hydrogencarbonates, carboxylates and gaseous CO are also detected at room temperature. Interestingly, the band for CO_x coordinated to the reduced state ceria appears at a lower temperature (150 °C), at the same time, a new band for gaseous CO₂ emerges at 2360 cm⁻¹, demonstrating that the reduction behavior of C2S1-450 is better than that of CeO₂-450, which is in accordance with H₂-TPR results. Moreover, the situation of C2S1-750 is very similar with C2S1-450, however, the bands for CO_x coordinated to the reduced state ceria and gaseous CO₂ appear at a higher temperature (200 °C). In summary, the reduction behaviors of these samples are following the order: C2S1-450 > C2S1-750 > CeO₂-450, suggesting that the incorporation of Sn⁴⁺ into the lattice of CeO₂ can improve its reduction behavior effectively, but the high-temperature calcination can weaken this promoting effect. However, the *in situ* DRIFTS result of CO adsorption on SnO₂-450 indicates that CO species cannot be adsorbed on the surface of SnO₂-450 under the current conditions, and we do not observe the reduction of SnO₂-450 by CO.

In order to understand the adsorption–desorption behaviors of these catalysts, the *in situ* DRIFTS of NO adsorption for the

representative samples recorded under high purified N₂ stream from 25 to 400 °C during the TPD process of NO are shown in Fig. 8. Exposing CeO₂-450 to NO at room temperature leads to some IR bands appear in the range of 1000–2000 cm⁻¹, the bridging bidentate nitrates display a NO₂ symmetric vibration mode at 1010 cm⁻¹ and a N=O stretching mode at 1605 cm⁻¹; the chelating bidentate nitrates exhibit two bands of symmetric and asymmetric vibration at 1237 and 1559 cm⁻¹, respectively; the linear nitrites give a vibration band at 1277 cm⁻¹; the bridging monodentate nitrates show a shoulder band at 1434 cm⁻¹; moreover, the gaseous NO molecules display a weak band at 1905 cm⁻¹ [25,46,50]. The introduction of high purified N₂ replacing NO into the DRIFTS cell at a rate of 5.0 ml min⁻¹ for 1 h does not change these IR bands except the disappearance of the band at 1905 cm⁻¹ for gaseous NO molecules. There are some obvious changes during the heating process: firstly, the band at 1277 cm⁻¹ for linear nitrites weakens with the increase of temperature and disappears at 350 °C due to its poor thermal stability; secondly, bridging monodentate nitrates (1434 cm⁻¹) can be eliminated at 200 °C; finally, the band at 1605 cm⁻¹ for N=O stretching mode of bridging bidentate nitrates gets weakened but not disappear even at 400 °C. However, the band at 1010 cm⁻¹ for NO₂ symmetric vibration mode of bridging bidentate nitrates, as well as the bands at 1237 and 1559 cm⁻¹ for symmetric and asymmetric vibration of chelating bidentate nitrates have no remarkable change during the heating process, indicating that they are very stable on the surface of CeO₂-450. With regard to the Sn⁴⁺-doped samples (C2S1-450 and C2S1-750), the vibration bands of bridging bidentate nitrates, chelating bidentate nitrates, linear nitrites, bridging monodentate nitrates and gaseous NO molecules can also be detected at the corresponding positions. The characterization results of these two samples are very similar with that of CeO₂-450. However, we can find that linear nitrites and bridging monodentate nitrates on the surface of C2S1-450 disappear at lower temperatures (200 and 150 °C, respectively). Similarly, the two kinds of adsorbed NO species on the surface of C2S1-750 can be eliminated at 250 and 200 °C, respectively. Furthermore, all the results indicate that these adsorbed NO species on the surface of C2S1-450 and C2S1-750 are easier to desorb/convert/dissociate than those on CeO₂-450 due to the more surface oxygen vacancies [19,20,51], which is supported by UV-Raman results. In addition, compared with CeO₂-450, we can notice that some of the vibration bands of adsorbed NO species on the surface of C2S1-450 and C2S1-750 shift to higher or lower wavenumber direction. This phenomenon can be explained by the synergistic interaction between Ce and Sn through the redox equilibrium of $2\text{Ce}^{3+} + \text{Sn}^{4+} \leftrightarrow 2\text{Ce}^{4+} + \text{Sn}^{2+}$, which causes the back-donation of the d-electron from the metal cation to the antibonding orbital of NO, this effect weakens the N–O bond [1]. In view of SnO₂-450, there are two bands attributed to linear nitrites and chelating bidentate nitrates located at 1286 and 1559 cm⁻¹ (25 °C), respectively. With the increase of temperature, these bands get weakened and a new band assigned to bridging bidentate nitrates appears at 1622 cm⁻¹ [50]. Compared with the above-mentioned three samples, we can find that the intensity of these bands for the adsorbed NO species on the surface of SnO₂-450 is considerably weak, demonstrating that the adsorption and activation effect of SnO₂-450 toward NO is quite poor.

With the purpose of clarifying the surface reaction situation of NO reduction by CO over these catalysts during the heating process, *in situ* DRIFTS of CO adsorption for the representative samples preadsorbed NO are collected at different temperatures, and the corresponding results are displayed in Fig. 9. Our previous works indicate that when exposing the ceria-containing sample to CO and NO mixed gases, NO molecules can preferentially adsorb on the surface of the sample due to their unpaired electrons and cover the active sites to inhibit the adsorption of CO molecules [6,9,25,27]. As a result, in the present work, the sample is exposed to a controlled

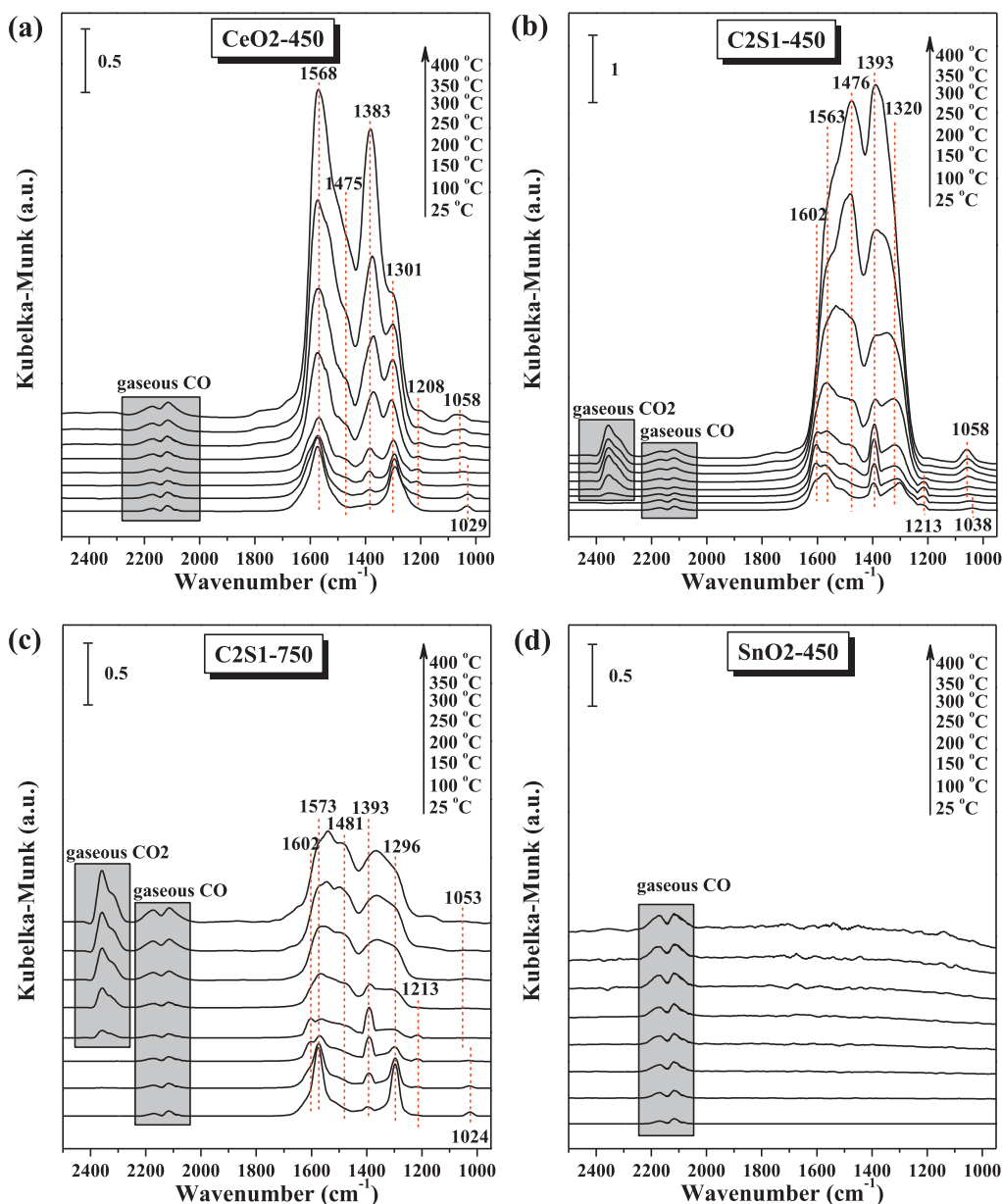


Fig. 7. *In situ* DRIFTS of CO interaction with the representative samples: (a) CeO₂-450, (b) C2S1-450, (c) C2S1-750 and (d) SnO₂-450.

stream of NO-Ar (5% of NO by volume) at a rate of 5.0 ml min⁻¹ for 1 h to be saturated firstly; and then the gaseous NO molecules are eliminated by using high purified N₂ stream; finally, the sample is exposed to a controlled stream of CO-Ar (10% of CO by volume) at a rate of 5.0 ml min⁻¹ for 1 h, and the corresponding *in situ* DRIFTS of CO adsorption for the sample are recorded under the same stream at a rate of 5.0 ml min⁻¹ during the heating process, which is similar with temperature programmed surface reaction (TPSR). It can be seen from Fig. 9a that although introducing CO molecules into the system of CeO₂-450 preadsorbed NO, there are only several kinds of nitrite-/nitrate-like species chemisorbed on the surface of CeO₂-450 without carbonates, hydrogencarbonates and carboxylates except for gaseous CO below 400 °C. Some interesting phenomena can be observed during the heating process: (1) all of the bands corresponding to the adsorption of NO species decrease to some extent with the temperature increasing to 300 °C. Simultaneously, gaseous CO₂ can be detected maybe due to the reduction

of CeO₂-450 and the adsorbed NO species; (2) further heating the sample to 400 °C, the adsorption of NO species disappear completely, carbonates and carboxylates can be found on the surface of CeO₂-450, because that the desorption/conversion/dissociation of adsorbed NO species expose active sites to adsorb CO species. Compared with CeO₂-450, these are some noticeable results for C2S1-450 in Fig. 9b: (1) gaseous CO₂ generates at a lower temperature (150 °C), indicating that the reduction of C2S1-450 and the adsorbed NO species on the surface of C2S1-450 is more easy; (2) similarly, the disappearance of adsorbed NO species and the appearance of adsorbed CO species can be observed at a lower temperature (300 °C), which may be due to that the more surface oxygen vacancies of C2S1-450 is beneficial to the dissociation of adsorbed NO species, and the improved reduction behavior of C2S1-450 can promote the formation of surface Ce³⁺ to adsorb CO species during the reaction process [19,20,22,23,51]; (3) the band at 2235 cm⁻¹ attributed to gaseous N₂O appears with the formation

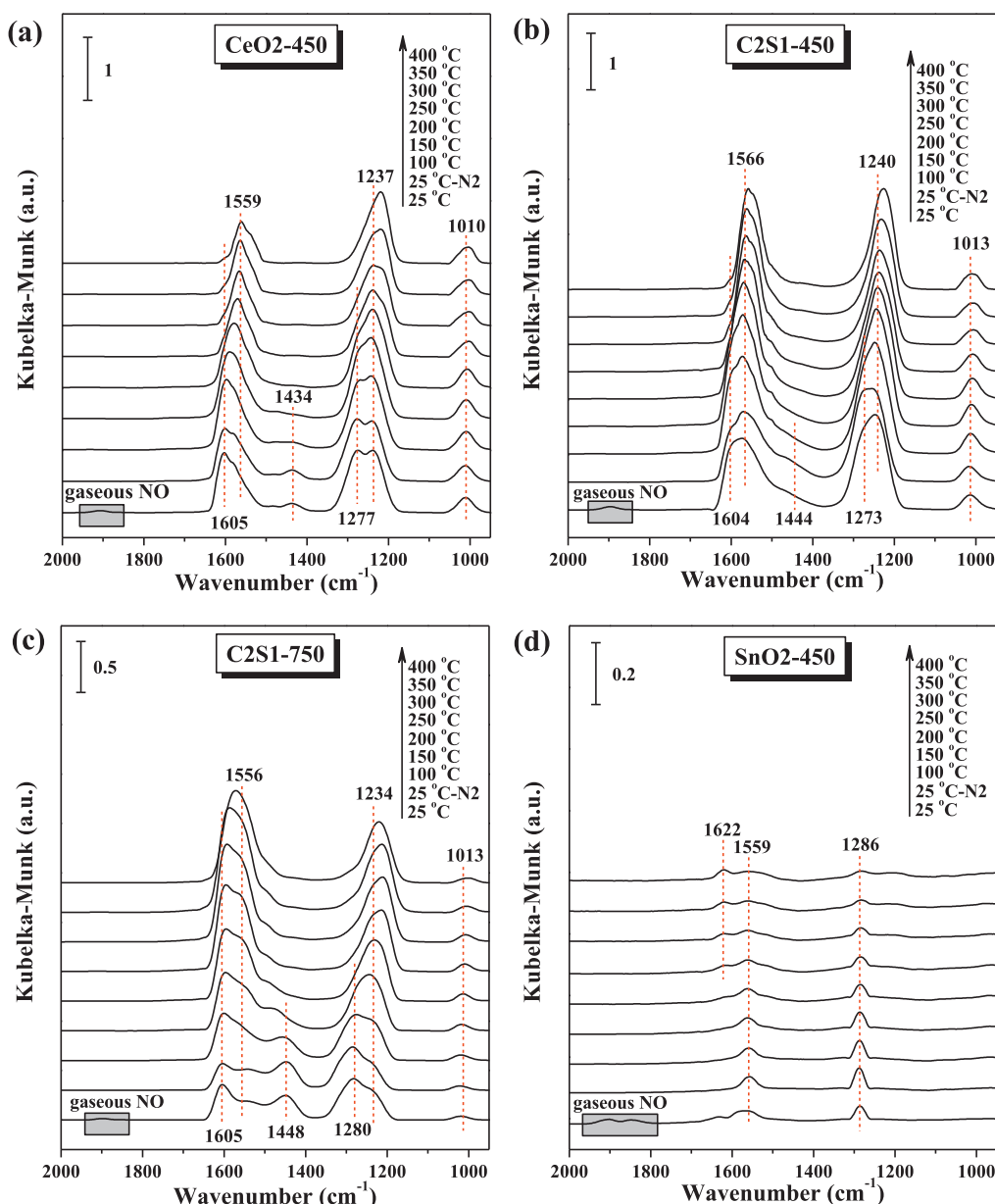


Fig. 8. *In situ* DRIFTS of NO interaction with the representative samples: (a) CeO₂-450, (b) C2S1-450, (c) C2S1-750 and (d) SnO₂-450.

of gaseous CO₂ at 150 °C, simultaneously, we can find that the band intensity of gaseous CO₂ for C2S1-450 is obvious stronger than that of CeO₂-450, demonstrating that NO reduction by CO model reaction can easier take place on the surface of C2S1-450, which is supported by the results of catalytic performance. Moreover, further increasing the temperature leads to the disappearance of gaseous N₂O owing to further reduced to N₂, which has no IR active mode because it is a diatomic homonuclear molecule [50]. By the same analysis method for Fig. 9c, we can find that the catalytic performance of C2S1-750 is inferior to that of C2S1-450 due to the sintering effect, but it is still better than that of CeO₂-450. With regard to SnO₂-450 (Fig. 9d), the obtained results are very similar with those of *in situ* DRIFTS of NO adsorption except the appearance of gaseous CO and gaseous CO₂ at 25 and 350 °C, respectively. Although the intensity of the bands for the adsorbed NO species is very weak, they do not disappear even at 400 °C, indicating that the adsorption and activation effect of SnO₂-450 toward NO is quite poor, so its catalytic performance is negligible under the current conditions.

3.7. Possible reaction mechanism of NO reduction by CO over these Ce_xSn_{1-x}O₂ mixed oxides

Based on the above-mentioned characterization results, a possible reaction mechanism of NO reduction by CO over these Ce_xSn_{1-x}O₂ mixed oxides under the current conditions is tentatively proposed to further understand the remarkable enhancement of the catalytic performance for this model reaction, as shown in Fig. 10. When exposing the Ce_xSn_{1-x}O₂ mixed oxide catalyst to CO and NO reaction mixture gases at room temperature, NO molecules are preferentially adsorbed on the surface of the catalyst due to their unpaired electrons to generate several kinds of nitrite and nitrate species, which further inhibit the adsorption of CO species [9,25]. However, the contact between CO molecules and the surface of Ce_xSn_{1-x}O₂ mixed oxide catalyst can lead to the reduction of the catalyst during the heating process to form more surface Ce³⁺ and oxygen vacancies. It is well known that the surface Ce³⁺ is conducive to the adsorption of CO species, and the surface oxygen vacancies can weaken the N–O bond to promote

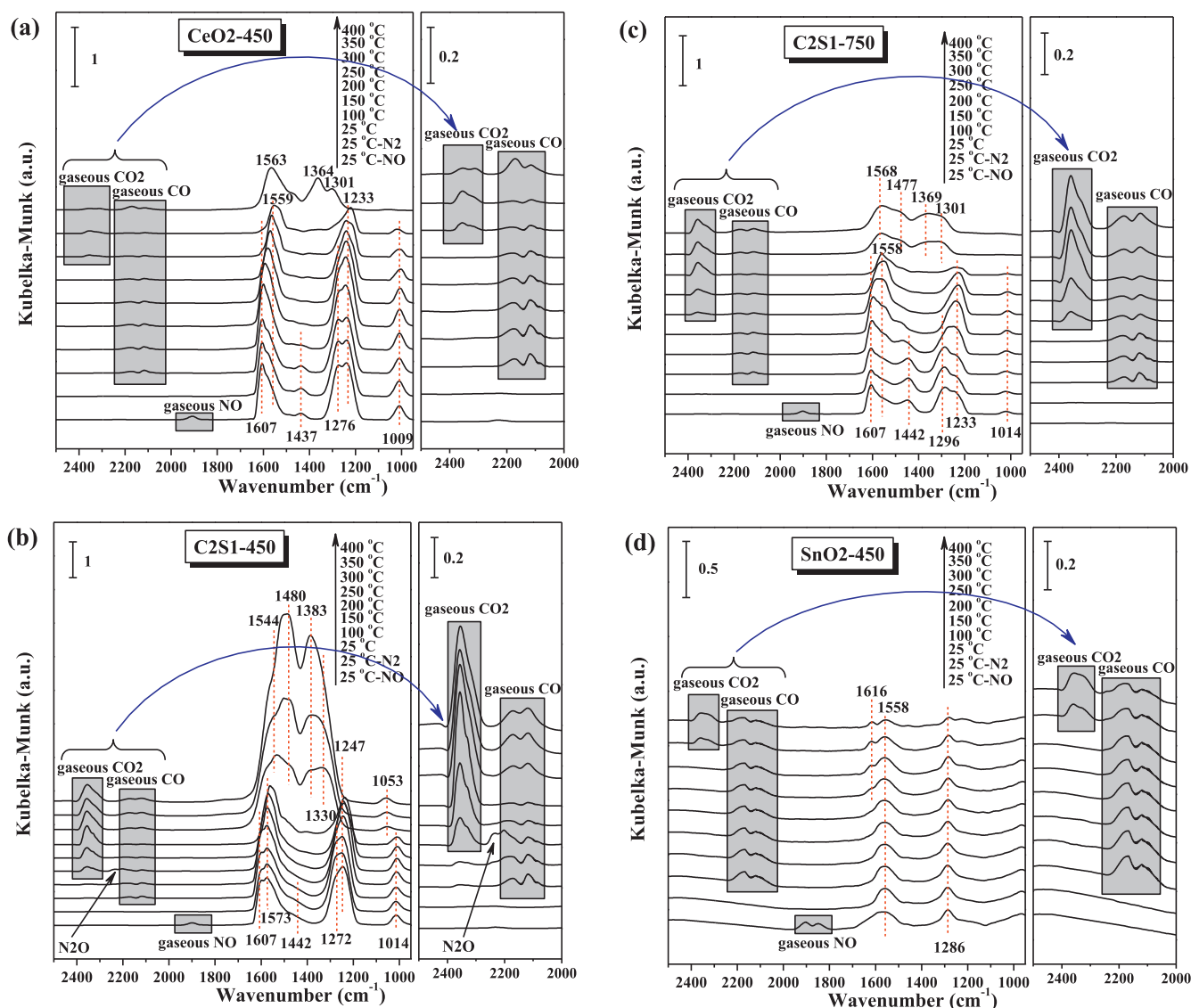


Fig. 9. *In situ* DRIFTS of CO interaction with the representative samples preadsorbed NO: (a) CeO₂-450, (b) C2S1-450, (c) C2S1-750 and (d) SnO₂-450.

the dissociation of NO species, which is further beneficial to the enhancement of the catalytic performance for NO reduction by CO model reaction [19,20,22,23,51]. Vividly, with the increase of temperature, the bridge oxygen of $-\text{Ce}^{4+}-\text{O}-\text{Ce}^{4+}-\text{O}-\text{Sn}^{4+}-\text{O}-\text{Sn}^{4+}-$ species in $\text{Ce}_x\text{Sn}_{1-x}\text{O}_2$ mixed oxide catalyst can be taken away by CO to generate $-\text{Ce}^{3+}-\square-\text{Ce}^{3+}-\square-\text{Sn}^{2+}-\square-\text{Sn}^{2+}-$ species (\square represents oxygen vacancy). CO species adsorbed on surface Ce^{3+} can react with O radicals resulted from the dissociation of NO species on the adjacent oxygen vacancy to produce CO₂, the rest N

radicals are able to combine with NO molecules to form N₂O, or their own combination to generate N₂. The by-product N₂O can be further reduced to N₂ at higher temperature. Interestingly, we can observe that there are three kinds of oxygen vacancy in $-\text{Ce}^{3+}-\square-\text{Ce}^{3+}-\square-\text{Sn}^{2+}-\square-\text{Sn}^{2+}-$ species: surface oxygen vacancy (SOV) of $-\text{Ce}^{3+}-\square-\text{Ce}^{3+}-$ and $-\text{Sn}^{2+}-\square-\text{Sn}^{2+}-$ species, as well as surface synergistic oxygen vacancy (SSOV) of $-\text{Ce}^{3+}-\square-\text{Sn}^{2+}-$ species [19]. With regard to $-\text{Ce}^{3+}-\square-\text{Ce}^{3+}-$ species, all the adjacent sites of oxygen vacancy are Ce^{3+} , which can adsorb CO species effectively. However,

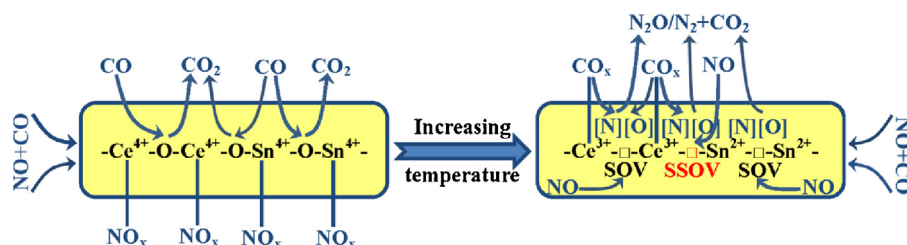


Fig. 10. Possible reaction mechanism for NO removal by CO over these $\text{Ce}_x\text{Sn}_{1-x}\text{O}_2$ mixed oxides, black \square : surface oxygen vacancy (SOV), red \square : surface synergistic oxygen vacancy (SSOV). (For interpretation of the references to color in this figure legend, the reader is referred to the web version of the article.)

the adsorption of CO species on surface Ce^{3+} can generate some steric effect for the dissociation of NO species on oxygen vacancy. In view of $-\text{Sn}^{2+}-\square-\text{Sn}^{2+}-$ species, its promoting role in NO reduction by CO model reaction is not very obvious, because that Sn^{2+} can't adsorb and activate the CO molecules efficiently, which is supported by *in situ* DRIFTS of CO adsorption. For $-\text{Ce}^{3+}-\square-\text{Sn}^{2+}-$ species, the adjacent sites of oxygen vacancy are Ce^{3+} and Sn^{2+} , the steric effect for the dissociation of NO species on oxygen vacancy would be smaller, because that Sn^{2+} can't adsorb CO species. As a result, we believe that the surface synergetic oxygen vacancy (SSOV) can enhance the catalytic performance more effectively than surface oxygen vacancy (SOV). Furthermore, the catalytic domain (CD, $-\text{Ce}^{3+}-\square-\text{Sn}^{2+}-$ species) in $\text{Ce}_x\text{Sn}_{1-x}\text{O}_2$ mixed oxide catalyst plays a key role in NO reduction by CO model reaction due to the synergistic effect between surface Ce^{3+} species and surface synergetic oxygen vacancy (SSOV).

4. Conclusions

In the present work, a series of $\text{Ce}_x\text{Sn}_{1-x}\text{O}_2$ mixed oxides and single oxides (CeO_2 and SnO_2) were prepared by inverse co-precipitation method with the purpose of investigating the correlation between the physicochemical properties and catalytic performances of these catalysts for NO reduction by CO model reaction. Combining with the above-mentioned characterization results, several conclusions can be obtained as follows:

- (1) The incorporation of Sn^{4+} into the lattice of CeO_2 leads to the decrease of crystallite size and the increase of lattice strain. The former can cause the enlargement of surface Ce^{3+} content and the increase of BET specific surface area, the latter is beneficial to the activation of reactant molecules, which further promote the enhancement of catalytic performance.
- (2) The reduction behaviors of these $\text{Ce}_x\text{Sn}_{1-x}\text{O}_2$ mixed oxides are improved compared with single oxides (CeO_2 and SnO_2), which is beneficial to the formation of more surface Ce^{3+} and oxygen vacancies in the reaction process, and further enhance the catalytic performance.
- (3) The catalytic domain (CD, $-\text{Ce}^{3+}-\square-\text{Sn}^{2+}-$ species) in these $\text{Ce}_x\text{Sn}_{1-x}\text{O}_2$ mixed oxides plays a key role in NO reduction by CO model reaction due to the synergistic effect between surface Ce^{3+} species and surface synergetic oxygen vacancy (SSOV).
- (4) The catalyst with the optimal mole ratio ($\text{Ce}:\text{Sn}=2:1$) exhibits the best catalytic performance for NO reduction by CO model reaction, because that more catalytic domains (CD, $-\text{Ce}^{3+}-\square-\text{Sn}^{2+}-$ species) can be generated in this sample due to the formation of uniform solid solution without crystalline SnO_2 blocking the active sites.

Acknowledgements

The financial supports of the National Natural Science Foundation of China (Nos. 20973091, 21273110), the National Basic Research Program of China (973 program, Nos. 2009CB623500, 2010CB732300), Jiangsu Province Science and Technology Support Program (Industrial, BE2011167), and Jiangsu Province Scientific Research Foundation for Graduate (No. CXZZ12.0038) are gratefully acknowledged.

References

- [1] Y.L. Fu, Y.C. Tian, P.Y. Lin, *Journal of Catalysis* 132 (1991) 85–91.
- [2] P. Granger, J.J. Lecomte, L. Leclercq, G. Leclercq, *Applied Catalysis A: General* 208 (2001) 369–379.
- [3] A.M. Pisanu, C.E. Gigola, *Applied Catalysis B: Environmental* 20 (1999) 179–189.

- [4] D. Na-Ranong, R. Yuangsawad, P. Kitchaiya, T. Aida, *Chemical Engineering Journal* 146 (2009) 275–286.
- [5] Y. Wang, A.M. Zhu, Y.Z. Zhang, C.T. Au, X.F. Yang, C. Shi, *Applied Catalysis B: Environmental* 81 (2008) 141–149.
- [6] X.J. Yao, Q. Yu, Z.Y. Ji, Y.Y. Lv, Y. Cao, C.J. Tang, F. Gao, L. Dong, Y. Chen, *Applied Catalysis B: Environmental* 130–131 (2013) 293–304.
- [7] R.D. Zhang, W.Y. Teoh, R. Amal, B.H. Chen, S. Kaliaguine, *Journal of Catalysis* 272 (2010) 210–219.
- [8] A.E. Giannakas, A.K. Ladavos, P.J. Pomonis, *Applied Catalysis B: Environmental* 49 (2004) 147–158.
- [9] X.J. Yao, C.J. Tang, Z.Y. Ji, Y. Dai, Y. Cao, F. Gao, L. Dong, Y. Chen, *Catalysis Science & Technology* 3 (2013) 688–698.
- [10] Q. Yu, X.X. Wu, C.J. Tang, L. Qi, B. Liu, F. Gao, K.Q. Sun, L. Dong, Y. Chen, *Journal of Colloid and Interface Science* 354 (2011) 341–352.
- [11] Y.J. Luo, Y.H. Xiao, G.H. Cai, Y. Zheng, K.M. Wei, *Applied Catalysis B: Environmental* 136–137 (2013) 317–324.
- [12] Z. Wang, G.L. Shen, J.Q. Li, H.D. Liu, Q. Wang, Y.F. Chen, *Applied Catalysis B: Environmental* 138–139 (2013) 253–259.
- [13] M. Guo, J.Q. Lu, Y.N. Wu, Y.J. Wang, M.F. Luo, *Langmuir* 27 (2011) 3872–3877.
- [14] J.L. Cao, Y. Wang, T.Y. Zhang, S.H. Wu, Z.Y. Yuan, *Applied Catalysis B: Environmental* 78 (2008) 120–128.
- [15] D.R. Sellick, A. Aranda, T. García, J.M. López, B. Solsona, A.M. Mastral, D.J. Morgan, A.F. Carley, S.H. Taylor, *Applied Catalysis B: Environmental* 132–133 (2013) 98–106.
- [16] W.T. Chen, K.B. Chen, M.F. Wang, S.F. Weng, C.S. Lee, M.C. Lin, *Chemical Communications* 46 (2010) 3286–3288.
- [17] M.F. Luo, J. Chen, L.S. Chen, J.Q. Lu, Z.C. Feng, C. Li, *Chemistry of Materials* 13 (2001) 197–202.
- [18] A.G. Makeev, N.V. Peskov, *Applied Catalysis B: Environmental* 132–133 (2013) 151–161.
- [19] D. Li, Q. Yu, S.S. Li, H.Q. Wan, L.J. Liu, L. Qi, B. Liu, F. Gao, L. Dong, Y. Chen, *Chemistry: A European Journal* 17 (2011) 5668–5679.
- [20] S.H. Oh, G.B. Fisher, J.E. Carpenter, D.W. Goodman, *Journal of Catalysis* 100 (1986) 360–376.
- [21] T. Baidya, A. Gupta, P.A. Deshpandey, G. Madras, M.S. Hegde, *Journal of Physical Chemistry C* 113 (2009) 4059–4068.
- [22] M. Boaro, F. Giordano, S. Recchia, V. Dal Santo, M. Giona, A. Trovarelli, *Applied Catalysis B: Environmental* 52 (2004) 225–237.
- [23] Z.X. Song, W. Liu, H. Nishiguchi, *Catalysis Communications* 8 (2007) 725–730.
- [24] S. Letichevsky, C.A. Tellez, R.R.D. Avilez, M.I.P.D. Silva, M.A. Fraga, L.G. Appel, *Applied Catalysis B: Environmental* 58 (2005) 203–210.
- [25] L.J. Liu, B. Liu, L.H. Dong, J. Zhu, H.Q. Wan, K.Q. Sun, B. Zhao, H.Y. Zhu, L. Dong, Y. Chen, *Applied Catalysis B: Environmental* 90 (2009) 578–586.
- [26] B.M. Reddy, A. Khan, P. Lakshmanan, M. Aouine, S. Loridant, J.C. Volta, *Journal of Physical Chemistry B* 109 (2005) 3355–3363.
- [27] X.J. Yao, F. Gao, Q. Yu, L. Qi, C.J. Tang, L. Dong, Y. Chen, *Catalysis Science & Technology* 3 (2013) 1355–1366.
- [28] L.J. Liu, Z.J. Yao, B. Liu, L. Dong, *Journal of Catalysis* 275 (2010) 45–60.
- [29] R. Si, Y.W. Zhang, S.J. Li, B.X. Lin, C.H. Yan, *Journal of Physical Chemistry B* 108 (2004) 12481–12488.
- [30] R. Kydd, W.Y. Teoh, K. Wong, Y. Wang, J. Scott, Q.H. Zeng, A.B. Yu, J. Zou, R. Amal, *Advanced Functional Materials* 19 (2009) 369–377.
- [31] L.Z. Liu, T.H. Li, X.L. Wu, J.C. Shen, P.K. Chu, *Journal of Raman Spectroscopy* 43 (2012) 1423–1426.
- [32] E. Fazio, F. Neri, S. Savasta, S. Spadaro, S. Trusso, *Physical Review B* 85 (2012) 195423.
- [33] T. Lan, C.W. Li, B. Fultz, *Physical Review B* 86 (2012) 134302.
- [34] K.S.W. Sing, D.H. Everett, R.A.W. Haul, L. Moscou, R.A. Pierotti, J. Rouquerol, T. Siemieniowska, *Pure and Applied Chemistry* 57 (1985) 603–619.
- [35] N. Acerbi, S. Golunski, S.C. Tsang, H. Daly, C. Hardacre, R. Smith, P. Collier, *Journal of Physical Chemistry C* 116 (2012) 13569–13583.
- [36] Y.Z. Chen, B.J. Liaw, C.W. Huang, *Applied Catalysis A: General* 302 (2006) 168–176.
- [37] M.F. Luo, J.M. Ma, J.Q. Lu, Y.P. Song, Y.J. Wang, *Journal of Catalysis* 246 (2007) 52–59.
- [38] L.X. Yin, Y.Q. Wang, G.S. Pang, Y. Koltypin, A. Gedanken, *Journal of Colloid and Interface Science* 246 (2002) 78–84.
- [39] L.J. Wu, H.J. Wiesmann, A.R. Mooney, R.F. Klie, Y.M. Zhu, D.O. Welch, M. Suenaga, *Physical Review B* 69 (2004) 125415.
- [40] R.K. Hailstone, A.G. DiFrancesco, J.G. Leong, T.D. Allston, K.J. Reed, *Journal of Physical Chemistry C* 113 (2009) 15155–15159.
- [41] V.M. Shinde, G. Madras, *Applied Catalysis B: Environmental* 138–139 (2013) 51–61.
- [42] P. Hartmann, T. Brezesinski, J. Sann, A. Lotnyk, J.P. Eufinger, L. Kienle, J. Janek, *ACS Nano* 7 (2013) 2999–3013.
- [43] M.S.P. Francisco, V.R. Mastelaro, P.A.P. Nascente, A.O. Florentino, *Journal of Physical Chemistry B* 105 (2001) 10515–10522.
- [44] G. Avgouropoulos, T. Ioannides, *Applied Catalysis B: Environmental* 67 (2006) 1–11.
- [45] K.I. Hadjiivanov, G.N. Vayssilov, *Advances in Catalysis* 47 (2002) 307–511.
- [46] Q. Yu, X.J. Yao, H.L. Zhang, F. Gao, L. Dong, *Applied Catalysis A: General* 423–424 (2012) 42–51.

- [47] F. Morales, E. de Smit, F.M.F. de Groot, T. Visser, B.M. Weckhuysen, *Journal of Catalysis* 246 (2007) 91–99.
- [48] L. Qi, Q. Yu, Y. Dai, C.J. Tang, L.J. Liu, H.L. Zhang, F. Gao, L. Dong, Y. Chen, *Applied Catalysis B: Environmental* 119–120 (2012) 308–320.
- [49] L.J. Liu, J.G. Cai, L. Qi, Q. Yu, K.Q. Sun, B. Liu, F. Gao, L. Dong, Y. Chen, *Journal of Molecular Catalysis A: Chemical* 327 (2010) 1–11.
- [50] K.I. Hadjiivanov, *Catalysis Reviews* 42 (2000) 71–144.
- [51] J.F. Chen, Y.Y. Zhan, J.J. Zhu, C.Q. Chen, X.Y. Lin, Q. Zheng, *Applied Catalysis A: General* 377 (2010) 121–127.